Received: 3 June 2020 | Revised: 11 February 2021 | Accepted: 5 March 2021

DOI: 10.1002/mrm.28782

FULL PAPER

Magnetic Resonance in Medicine

Analysis and mitigation of noise in simultaneous transmission and reception in MRI

Bilal Tasdelen[1,2] | **Alireza Sadeghi-Tarakameh**[1,2] | **Ugur Yilmaz**[2] | **Ergin Atalar**[1,2]

[1]Department of Electrical and Electronics Engineering, Bilkent University, Ankara, Turkey

[2]National Magnetic Resonance Research Center (UMRAM), Bilkent University, Ankara, Turkey

Correspondence
Ergin Atalar, Department of Electrical and Electronics Engineering, Bilkent University, Ankara 06800, Turkey.
Email: ergin.atalar@bilkent.edu.tr

Purpose: In simultaneous transmission and reception (STAR) MRI, along with the coupling of the excitation pulse to the received signal, noise, and undesired distortions (spurs) coming from the transmit chain also leak into the acquired signal and degrade image quality. Here, properties of this coupled noise and its relationship with the transmit amplifier gain, transmit chain noise density, isolation performance, and imaging bandwidth are analyzed. It is demonstrated that by utilizing a recently proposed STAR technique, the transmit noise can be reduced. The importance of achieving high isolation and careful selection of the corresponding parameters are demonstrated.

Theory and Methods: A cancellation algorithm, together with a vector modulator, is used for transmit-receive isolation. The scanner is modeled as a pipeline of blocks to demonstrate the noise contribution from each block. With higher isolation, coupled transmit noise can be reduced to the point that the dominant noise source becomes acquisition noise, as in the case for pulsed MRI. Amplifiers with different gain and noise properties are used in the experiments to verify the derived noise-transmit parameter relation.

Results: With the proposed technique, more than 80 dB isolation in the analog domain is achieved. The leakage noise and the spurs coupled from the transmit chain, are reduced. It is shown that the transmit gain plays the most critical role in determining sufficient isolation, whereas the amplifier noise figure does not contribute as much.

Conclusion: The transmit noise and the spurs in STAR imaging are analyzed and mitigated by using a vector modulator.

KEYWORDS

active cancellation, receive noise, STAR, transmit noise

1 | INTRODUCTION

In this work, we analyzed noise and spurs leaking from the transmit chain to the receive chain and derived the relation between signal-to-noise ratio (SNR) and the transmit chain parameters (eg, noise performance and gain) during simultaneous transmission and reception (STAR) imaging in MRI. This leakage, containing coupled excitation signal, transmit noise and spurious signals, degrades image quality, and should be isolated. We have shown that by using an active cancellation circuit and a control algorithm, it is possible to isolate the leakage and the noise coming from it.

In pulsed MRI, acquisition and excitation happen in distinct times, exploiting the slow signal decay of the tissues.[1,2] This feature simplifies the system greatly by circumventing the issue of self-interference. Due to its convenience and flexibility, pulsed MRI methods are well investigated and widely used over the years. However, pulsed MRI has its disadvantages, such as having a dead time between transmission and reception, during which NMR signal decays. Signal decay is more prominent with the specimens that have low T_2 values, including tissues such as bones, ligaments, and teeth.[3] Although there are pulse sequences specifically designed for imaging such tissues (eg, UTE,[4,5] ZTE,[6-10] SWIFT[11,12]), they are hardware demanding in terms of fast transmit/receive switching or high slew-rate gradients. Some of them may produce high acoustic noise, or deposit high RF power to the body.

An alternative technique is the STAR imaging, which reduces signal loss since the dead time can be eliminated.[13-17] This method also has the advantage of acquiring the signal from the tissues with very short T_2 values. There is no need for fast switching gradients in this method implying reduced acoustic noise.[15] Moreover, it is shown that this method requires much less RF power compared to similar nonsimultaneous techniques (eg, continuous SWIFT vs. SWIFT).[13,17]

Even though STAR imaging carries the advantages mentioned above, several issues hinder the possibility of clinical usage. Self-interference is the primary consideration that requires handling. Self-interference is time-varying in nature, mostly due to the load and environment variations. It reduces the dynamic range of the receive chain, even to the point of saturation, if unchecked. Another challenge, closely related to the self-interference issue, is the injection of the transmit noise and spurs (undesired peaks in the spectrum) into the received signal. Because of this issue, the transmit amplifiers of the scanners are usually replaced with low-noise, low-power amplifiers.

There are many active and passive approaches proposed to overcome the self-interference issue. Passive methods such as geometric decoupling[18] and decoupling matrix[19,20] are already common for the receive-receive isolation and the transmit-transmit isolation, and they can be used for the transmit-receive isolation as well.

For active cancellation, there are several methods proposed both in telecommunications[21,22] and in MRI.[13–15,23] Although these methods introduce complexity, are inefficient in terms of power, and require specialized hardware, they are necessary to compensate for the time-varying part of the leakage signals. The method proposed in Ozen et al[14] uses 2 independent transmit sources, which introduces an uncorrelated noise source, whereas methods in Sohn et al,[13] Ozen et al,[15] and the method used in this paper samples the compensation signal from the main transmit signal. The proposed method here, similar to Salim et al,[16] uses a digitally controlled vector modulator; however, the other works[13,15] employ voltage-controlled modulators using active devices.

The transmit noise and the spurs that leak to the received signal reduce the SNR and introduce artifacts. Cancellation methods in the analog domain (as opposed to cancellation in post-processing)[13,15,24] isolate the transmit noise since it is highly correlated to the noise on the compensation signal.[25-27] This correlation implies there is a direct relation between SNR and isolation. Furthermore, the importance of obtaining high isolation is known for increased dynamic range; however, isolation and SNR relation requires further analysis.[28]

In this work, transmit noise and spurs issues, and the trade-off between the transmit chain parameters (gain and noise) that govern the relation between SNR and isolation are investigated. STAR imaging is realized by utilizing a combination of a passive and an active method to verify the findings. For passive isolation, electrical isolation between the ports of a birdcage coil is exploited. Moreover, a technique recently proposed by the authors of this paper is used, which enables a fast and convenient way for active isolation.[24] The algorithm and hardware used for active compensation are detailed and its merit for reducing the coupled transmit noise is demonstrated.

2 | THEORY

2.1 | Signal description

With the inclusion of the self-interference, acquired signal $s_{\mathrm{Rx}}(t)$ can be described as in Equation (1).

$$s_{\mathrm{Rx}}(t) = s_{\mathrm{MR}}(t) + n_{\mathrm{acq}}(t) + A(t)\cdot e^{i\phi(t)}\cdot \bar{s}_{\mathrm{Tx}}(t) \tag{1}$$

Here, $\bar{s}_{\mathrm{Tx}}(t)$ is the distorted transmit pulse mainly leaked due to the coupling effect between the transmit and receive coil. It can be further expanded as $\bar{s}_{\mathrm{Tx}}(t) = s_{\mathrm{Tx}}(t) + \varepsilon + n_{\mathrm{Tx}}(t)$, where $s_{\mathrm{Tx}}(t)$ is the ideal RF pulse, ε is the spurs (or spurious tones originating from the quantization errors in digital frequency synthesis) and distortions added to the pulse and $n_{\mathrm{Tx}}(t)$ is the transmit noise. $A(t)$ and $\phi(t)$ are time-varying amplitude and phase modulations on $\bar{s}_{\mathrm{Tx}}(t)$ occurring due to load variations, temperature change, vibrations, etc. $n_{\mathrm{acq}}(t)$ is the receive noise, which in pulsed MRI is the only noise source in the system. It will remain even if the other noise sources in the STAR imaging is eliminated. As described by Idiyatullin et al[11] and Garwood et al,[29] MRI signal, $s_{\mathrm{MR}}(t)$ can be written as:

$$s_{\mathrm{MR}}(t) = i(\mathscr{M}(\boldsymbol{k}(t)) * s_{\mathrm{Tx}}(t)) \tag{2}$$

This equation holds for the small tip angle approximation under constant gradients, which corresponds to an inside out

($k(t) \geq 0$) radial trajectory. Here, $*$ represents the convolution operation, and $\mathcal{M}(\boldsymbol{k}(t))$ is the magnetization in the spatial frequency domain. Thus, $\mathcal{M}(\boldsymbol{k}(t))$ can be obtained by deconvolving the excitation pulse $s_{\mathrm{Tx}}(t)$ from the acquired signal $s_{\mathrm{MR}}(t)$.

2.2 | Decoupling algorithm

In literature, to find the inputs that will minimize the leak signal, usually searching algorithms such as gradient descent and genetic algorithms are used.[15,23] These approaches work well, especially if the problem has a small number of degrees of freedom and does not have many local minima. For some circuits as used in Salim and Atalar,[23] the problem becomes quite complex with an abundance of local minima and a high number of degrees of freedom. Convergence time drastically increases with this complexity. In both cases, reaching a good solution with fewer iterations is important since the measurement is costly. In Bharadia et al,[21] a look-up table (LUT)–based algorithm is utilized, which finds a good initial point for gradient descent, increasing the convergence rate. Our approach is to extend this idea (storing the circuit behavior) by characterizing the circuit via measurements once and using this LUT to find a minimum point. Hence, it is possible to decrease further the time required to find a minimum point since the need for acquiring measurements for every subsequent input is eliminated. Thus, to enable these benefits by using the LUT instead of the measurements, the behavior of the circuit is modeled and the output of the circuit for a given control input is estimated.

With the linearity assumption, the input-output relationship of the vector modulator can be written as in Equation (3) in the frequency domain:

$$Y(f,\boldsymbol{x}) = H(f,\boldsymbol{x}) \cdot X(f) \tag{3}$$

where the $\boldsymbol{x}$ is the control input vector to the vector modulator, $H(f,\boldsymbol{x})$ is the transfer function that is also dependent on the control inputs, $Y(f,\boldsymbol{x})$ is the output, and $X(f)$ is the input. For a known initial $H(f,\boldsymbol{x_0})$, by measuring the output $Y(f,\boldsymbol{x})$, input $X(f)$ can be found. Once $X(f)$ is known, from Equation (3), the output can be inferred for any $\boldsymbol{x}$, with the knowledge of $H(f,\boldsymbol{x})$.

For a leak signal $Y_l(f)$, estimated residual signal amplitude after the cancellation can be written as $\hat{\epsilon} = |Y_l(f) - \hat{Y}(f,\boldsymbol{x})|$ and the cancellation problem becomes $\min_{\boldsymbol{x}} |\hat{\epsilon}|$. Note that the expected residual signal amplitude $\hat{\epsilon}$ can be considered as the quantization error caused by the quantized nature of $\boldsymbol{x}$. A source of error that increases the final true residual amplitude ϵ is the disparity between estimation $\hat{H}(f,\boldsymbol{x})$ and $H(f,\boldsymbol{x})$. Thus, to be able to attain high isolation (eg, an additional 50 dB), the relative error of the estimated $\hat{H}(f,\boldsymbol{x})$ to the true $H(f,\boldsymbol{x})$ needs to be small. Estimations solely based on simulations and manufacturer-supplied information are not reliable enough. Our algorithm relies on the characterization measurements and a compensation loop that removes the bias and minimizes the error by iterating over a set of candidate points found from the LUT to circumvent this issue. If a selected candidate fails to meet the threshold, we assume either the coupling has changed, or our estimation of circuit output was off in the previous step. Hence we estimate the residual and try a new candidate again until the threshold is achieved. For this paper, since taking care of frequency dependency of the hardware would increase the complexity, all of the measurements and estimations are done for a single frequency (f_0). This trade-off deemed fair since the frequency response of the leak signal is flat around the center frequency of the scanner. Further details regarding the description and derivation of the cancellation process are given in the Appendix.

2.3 | Noise and spurs

The general strategy on STAR imaging in MRI is to isolate the transmit and receive coils on the analog domain as much as possible and then remove residual leak signal during image reconstruction by utilizing digital subtraction methods. Having higher isolation is beneficial in terms of increased dynamic range and reduced artifacts that stem from imperfect digital subtraction. Although achieving isolation high enough to suppress the leak below the noise floor is theoretically possible, preserving this isolation throughout imaging is not always feasible. Hence, having a metric to determine sufficient isolation to achieve the desired SNR value is essential, especially for designing hardware for active cancellation.

In the case of STAR imaging, the dominant noise sources can be listed as white noise that is mostly stemming from the thermal noise of transmit chain elements,[30] the phase noise primarily originating from the signal synthesizer of the spectrometer, and further emphasized by the devices that have nonlinear behavior,[31-33] spurs that consist of undesired frequency peaks arising from external interference coupled to transmit path and the quantization process of the spectrometer.[34]

In conventional imaging, in the absence of the noise sources above, received noise power at room temperature, which corresponds to the noise level at the input of the receive chain (power spectral density of $n_{\mathrm{acq}}(t)$ from Equation (1)) will be close to the noise floor and can be written as:

$$N_{\mathrm{acq}}(f) = k \cdot T \cdot F_{\mathrm{LNA}} \cdot G_{\mathrm{LNA}} \tag{4}$$

Here, G_{LNA} and F_{LNA} are the overall gain and noise factor of the low-noise amplifier (LNA), respectively. k is the Boltzmann constant and T is the temperature of the body. This quantity can also be considered the minimum achievable noise power density for STAR imaging, that is, the noise level of conventional imaging.

To understand the relationship between the transmit parameters and SNR, it is assumed that the transmit chain noise at the output of the STAR circuit is perfectly correlated to the transmit chain noise at the output of the receive coil, that is, the amount of cancellation achieved for the signal is also the amount of cancellation achieved for the noise. Also, it is assumed that no other noise is coupled to the system after the transmit chain. Failure of these assumptions will result in an underestimation of the noise power. With these assumptions, the total received noise N_{sys} can be calculated as:

$$N_{sys} = N_{acq} + ((N_{Tx} \cdot G_{comp} + N_{comp}) \cdot G_{LNA} + N_{LNA}) \quad (5)$$

$$N_{Tx} = N_{Spec} \cdot G_{PA} + N_{PA} \quad (6)$$

The magnitude of final coupling obtained by the combination (sum of the complex gains) of the coil's coupling coefficient and vector modulator's output is denoted as G_{comp}. Here, G_{PA} and G_{LNA} are the available power gain (or attenuation) of the transmit power amplifier (PA) and the LNA, respectively. Similarly, N_{Spec}, N_{PA}, N_{comp}, and N_{LNA} are the output referred noise power of the spectrometer, the transmit amplifier, the vector modulator, and the LNA, respectively. Observing Equations (4) and (5), thermal noise floor kT can be chosen as the acceptable noise level which will incur at most 3 dB transmit noise impact on the image.

$$G_{comp} \leq \frac{kT}{N_{Spec} \cdot G_{PA} + N_{PA}} \quad (7)$$

As expected, sufficient isolation is directly related to the multiplication of the spectrometer's noise output (ie, input noise) and gain, as well as the noise output of the amplifier. Although not shown in the equation, gains (and possibly noise power spectrum due to the filters employed in the scanner) are dependent on the frequency, hence play an essential role. Considering bandwidth of the G_{comp} is quite narrow (7 kHz for -80 dB bandwidth), sufficient isolation needs to be determined by the lowest isolation in the imaging bandwidth. Thus, imaging bandwidth is also a parameter here.

3 | METHODS

3.1 | Hardware

The hardware consists of a vector modulator[16] and Wilkinson divider/combiner to sum the modified transmit signal with the received signal. The combined signal at the output of the Wilkinson combiner is measured via scanner and sent to a remote computer, where the cancellation algorithm resides. Cancellation codes (inputs of the vector modulator) determined by the remote computer are sent to a mini-computer (Raspberry Pi 3B+) placed in the scanner room via an optical link that translates the inputs into SPI protocol to program the attenuators in vector modulator. A detailed schematic of the overall system is given in Figure 1.

There are 4 lines with distinct fixed phase shifts in the vector modulator, and the magnitude of each line can be set by a digital step attenuator (DSA). 7-bit 0.25-dB step DSAs are used (PE43705A, Peregrine Semiconductors). The vector modulator has a 0.1-dB compression point at 40 dBm and it can handle 34 dBm of continuous-wave input power. In the ideal case where there is no reflection between the stages of the circuit, and there is infinite isolation between the dividing branches of the dividers, the output of the vector modulator is simply the complex sum of each branch, multiplied by the complex attenuation factor that is determined by the current state of the attenuators. In this work, this assumption will be used to estimate the output of the circuit. Failure in this assumption is not critical since it has the same effect as the coupling between the coils and results in a higher residual signal than expected. This is the leading cause of the cancellation error and can be corrected with the same circuit via the proposed algorithm.

A custom-made two-port 16-rung high-pass birdcage coil is designed using the co-simulation method.[35,36] It is used as a transceiver with around -20 dB reflection at the ports and less than -35 dB coupling between its ports. Together with the birdcage coil and the proposed vector modulator, around 50 dB isolation can be achieved in the 250 kHz bandwidth around the center frequency of 123.3 MHz. For power division and combination, topology proposed by Okada et al[37,38] is used.

3.2 | Imaging and noise experiments

Imaging experiments were conducted on a 3T Siemens Tim Trio scanner (Siemens Medical Solutions, Erlangen, Germany). The imaging sequence consisted of the calibration and imaging parts. The calibration part ran first and sampled the leakage by simultaneously transmitting and receiving. After the predetermined isolation threshold was surpassed, the image was acquired similar to the cSWIFT sequence. For excitation, Tukey windowed chirp pulses were used.[12] Gradients were not ramped down after the acquisition, both to reduce acoustic noise and vibrations due to gradient switching, and to crush the remaining signal before the next TR.

For the transmit RF pulse, power was set to 25 mW regardless of the pulse duration. The nutation frequency was estimated as $2^\circ\,\mathrm{ms}^{-1}$ by averaging over a region of interest in the middle of the phantom using a simulated B_1 map of the birdcage coil.

Image reconstruction was performed by first deconvolving, and then applying bullseye filtering as described by Corum et al.[39] Deconvolution is performed in the frequency

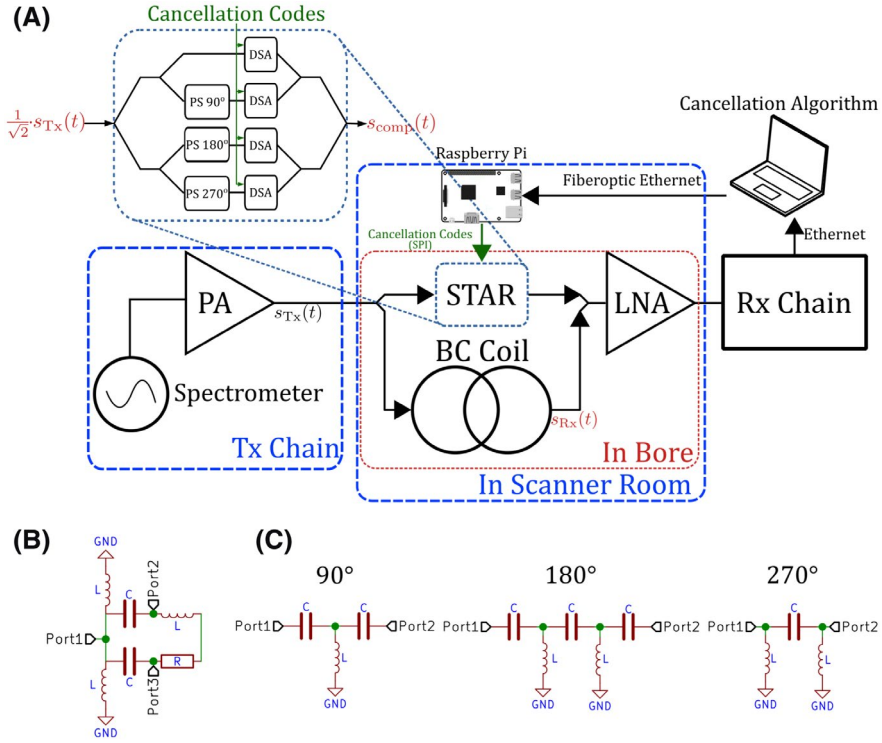

FIGURE 1 Schematic description of the STAR system and the MRI scanner. A, Overall system diagram. Measurements are read from the scanner after digitization via real-time data transfer functionality. B, Implementation of the Wilkinson power divider/combiner as proposed in Okada et al.[38,38] Power division ratio of −3 dB (equal) was used for all of the dividers/combiners. C, Implementation of the fixed phase shifters

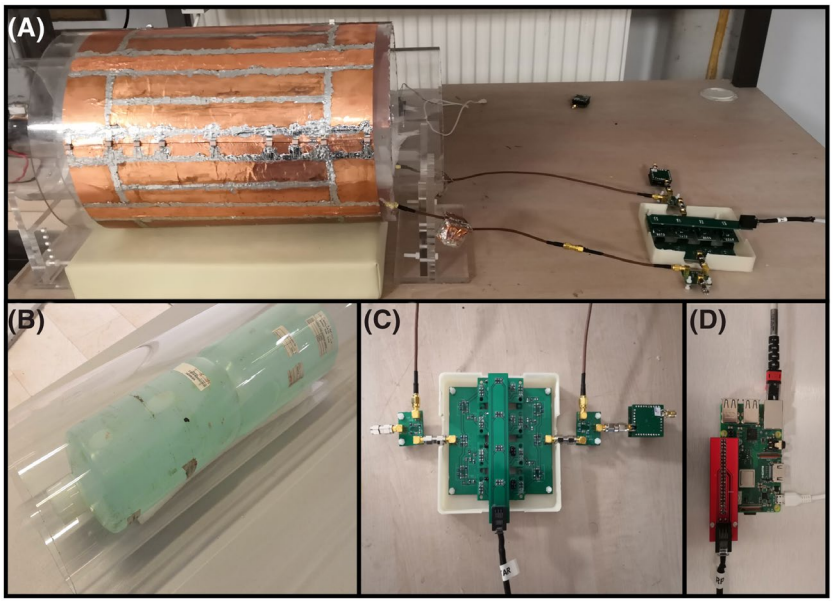

FIGURE 2 Photographs of the experiment setup. A, Overall experiment setup. B, Phantoms and their placements. C, Vector modulator. Circuit is connected to the coil, and the power amplifier and the LNA via Wilkinson power dividers/combiners. D, Raspberry Pi 3B+ powers and communicates with the vector modulator

domain by Wiener deconvolution. For the noise spectrum, white Gaussian noise is assumed, the spurs and residual transmit signal are ignored in the deconvolution process. The noise power is estimated via inspection of the acquired data. Note that one can compromise from resolution to reduce noise and artifacts from the final image by considering the effect of spurs and residual. Finally, deconvolved and filtered radial k-space data were reconstructed to the 3D volume via gridding[40] and inverse Fourier transform.

Two jar-shaped $CuSO_4$ phantoms (Siemens Medical Solutions, Erlangen, Germany) were placed in the birdcage coil so that their bottoms are barely touching each other, as can be seen in Figure 2B. This placement was done to load the coil and mimic the knee since the coil is designed for knee imaging. It was attempted to place the middle of 2 phantoms at the isocenter by adequately positioning the coil inside the bore. FOV was set to 300 mm in the radial direction. A larger FOV might be needed to avoid aliasing due to the signal coming from low T_2 materials, including the coil frame in the case a larger imaging bandwidth is used. However, since the imaging bandwidth was low, only the signal from the phantoms was detected, and no aliasing occurred with this FOV.

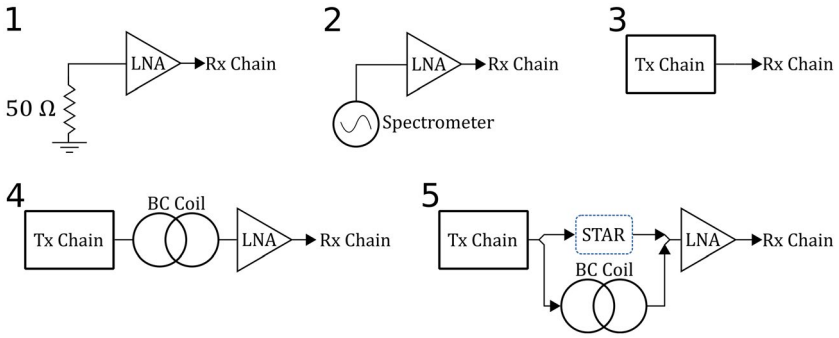

FIGURE 3 Schematics of the noise experiments. Experiments 3, 4, and 5 are repeated for LPA and HPA. An attenuator of known value (−25 dB) after the transmit chain is used when necessary to protect the receive chain from saturation and damage

For noise experiments, the noise power density at the output of each component was estimated. Noise contributions were investigated as output referred noise power N, which can be calculated in terms of noise factor F and gain G of the device under test (DUT).

In the noise experiments, 2 different transmit amplifier combinations were used. The first amplifier, which was referred to as a low-gain power amplifier (LPA) in this paper, was custom-designed using a low-noise power amplifier chip (GRF5020, Guerilla RF). The chip has around 28 dB gain, 2 dB noise figure, and OP1dB of 27 dBm. The second setup was called as high-gain power amplifier (HPA), and it was the cascade of 2 LPA, which amounts to 55.5 dB gain, 2 dB noise figure, and OP1dB of 27 dBm. A network analyzer (E5061B, Agilent) and a noise figure meter (8970B, HP) were used for gain and noise figure measurements.

Output referred noise power was inferred from the measurements to characterize the system using a spectrum analyzer (N9913A, Agilent). A continuous sinusoidal wave at the frequency of 123.25 MHz with −45 dBm power sent to all of the amplifiers. Output powers of the LPA and HPA were measured as approximately −17 and 10.5 dBm, respectively. The measurements were done according to the modeled experiments in Figure 3. A 25-dB attenuator was used at the output of the signal generator where necessary to keep the amplitude of the received signal in the receiver's dynamic range. At the receiver side of the spectrum analyzer, power spectrum within 200 kHz bandwidth around the center frequency is recorded. Resolution bandwidth of 150 Hz and 8 averaging is used. Noise experiments were performed in the Faraday cage to minimize the effect of the external noise. Noise only parts of the acquired spectrum closer to the center frequency was manually selected and power spectral density (PSD) of the noise was calculated.[41]

4 | RESULTS

4.1 | Isolation and imaging

Results related to isolation performance are given in Figure 4. Due to the nature of the algorithm, at some iterations increase in the leak signal was observed; however, −80 dB isolation threshold was successfully achieved eventually (G_{comp} was less than −80 dB).

Acquired images with the system can be seen in Figure 5. Bullseye artifacts stemming from the RF and the radial sampling imperfections were mostly reduced with bullseye filtering. Visible disturbances on the signal occurred due to the vibrations were eliminated by adding a dead time after gradient switching.

Images with 2.56 kHz bandwidth suffered from susceptibility artifacts but exhibited fewer artifacts due to residual leak signal. Also, artifacts were more prominent at the middle slices, whereas in the periphery, they diminished, which is due to the nature of the leak after the deconvolution. Furthermore, the number of spokes was halved for low bandwidth images since scan time was prohibitively long. Thus, streaking artifacts occurred due to undersampling.

Additional bullseye artifacts were observed in the images due to the timing issue of the RF pulse, which was also seen on raw data. The duration of the intended RF pulse and the actual RF pulse were different. This difference was corrected by stretching the RF pulse in time while the middle part is stationary. Then, the modified RF pulse was used in deconvolution, which eliminated these bullseye artifacts.

4.2 | Noise experiments

Measured output referred noise powers, and gains of the blocks can be seen in the schematic in Figure 6. Calculated values are consistent with the network analyzer and noise figure measurements.

White noise spectral density measurements is present can be seen in Table 1. The minimum achievable noise power measurement of experiment 1 was consistent with the calculated value using Equation (4) with a 0.2 dB variation. Rest of the measurements are in good agreement with calculated values for LPA and HPA.

Lastly, the PSD of the experiments can be seen in Figure 7. Spurs, phase noise, and leak signal isolation behaved as expected. Band-stop characteristic of the active cancellation can be observed in the noise spectrum of Figure 7C, HPA

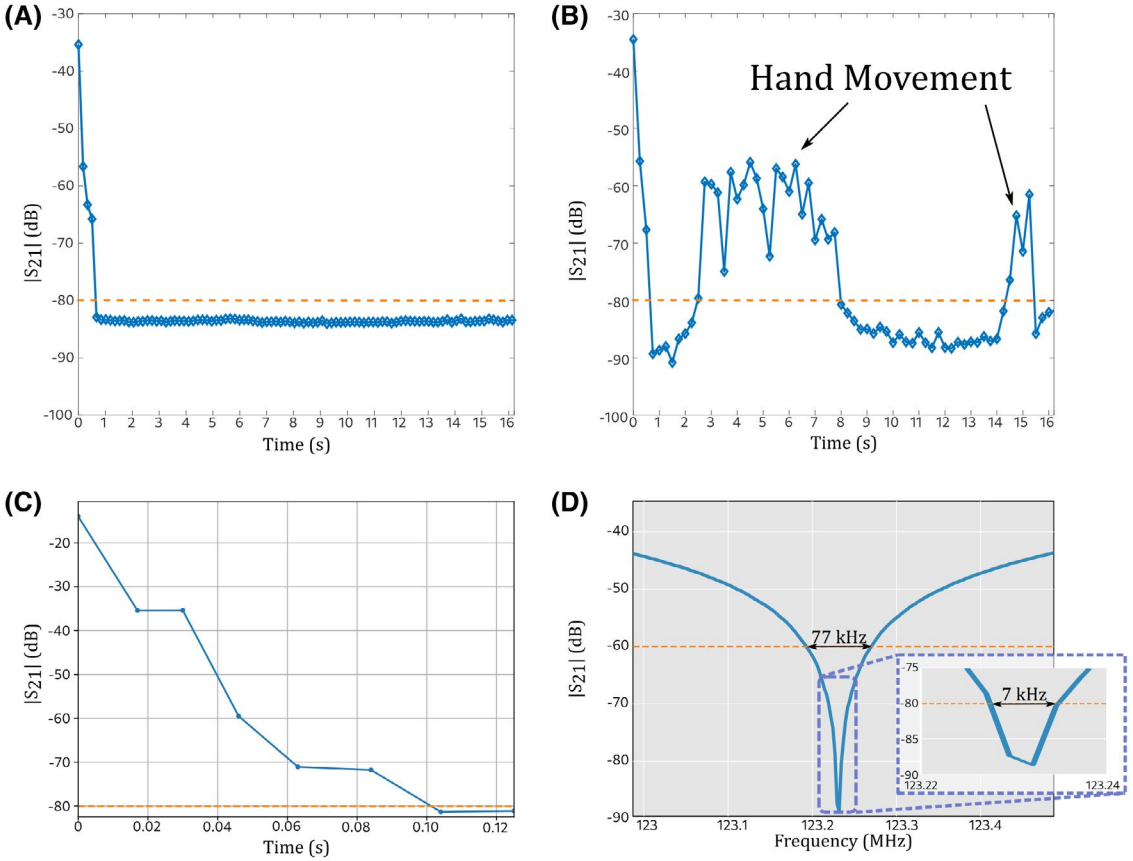

FIGURE 4 Isolation performance graphics. A, Network analyzer experiment in a stable environment (eg, load is static, no vibration around coil, etc.). B, Same experiment with (A), but this time hand movement is present in the vicinity of the coil. C, Decoupling performance in MRI scanner. Note that, due to vector modular output being higher than the leak signal, initial value for isolation does not represent passive cancellation. D, G_{comp} ($|S_{21}|$) of the actively isolated system and its −60 and −80 dB bandwidth values

measurement. For both of the amplifiers, as the result of active cancellation, noise level around the center frequency reduced back to the minimum achievable noise power.

5 | DISCUSSION

In STAR imaging, transmit noise also plays a vital role in determining the SNR. Transmit noise can be considered as the noise input to the transmit system (generated by spectrometer) multiplied by the transmit gain and the additional contributions of other noise generating elements (amplifiers and the cancellation circuit) as summarized in Equation (5). With proposed cancellation hardware, it is shown that it is possible to isolate the transmit noise in addition to the leak signal for a given transmit gain, consistent with the works by Montanari et al,[25] Zhou et al,[26] and Emara et al.[25]

Following the relationship between isolation, noise, and transmit chain parameters given in Equation (7), sufficient isolation can be calculated to reduce the noise to the receive noise level or minimum achievable noise level. Minimum possible noise is emphasized as the threshold since it eliminates the SNR disadvantage of STAR over the conventional imaging. After reducing the excess noise, digital subtraction methods can be used in post-processing to remove the residual leak.

Isolation can be further increased to recover the reduced dynamic range and suppress the artifacts due to the imperfect digital subtraction. It is also possible that, with higher isolation, higher gain amplifiers can be used for STAR imaging without increasing the received noise too much. Furthermore, using higher gain without increasing additive noise due to the transmit chain may enable a higher flip angle, which in turn, can yield better SNR. On the other hand, reducing sufficient isolation can also be preferred in some applications to reduce the circuit complexity and cost, as well as the algorithm memory consumption. A lower gain transmit amplifier can be used, or a spectrometer with lower noise output can be used to relax the required isolation. 25 mW power output used in this work allowed us to mitigate the transmit noise in the meantime provided sufficient nutation frequency for cSWIFT imaging with a knee coil. In the case of body imaging with bigger coils, higher power output might be necessary.

In this work, the limiting factor on the achievable isolation in a given imaging bandwidth was the isolation bandwidth. In the future, higher cancellation bandwidth is needed to achieve

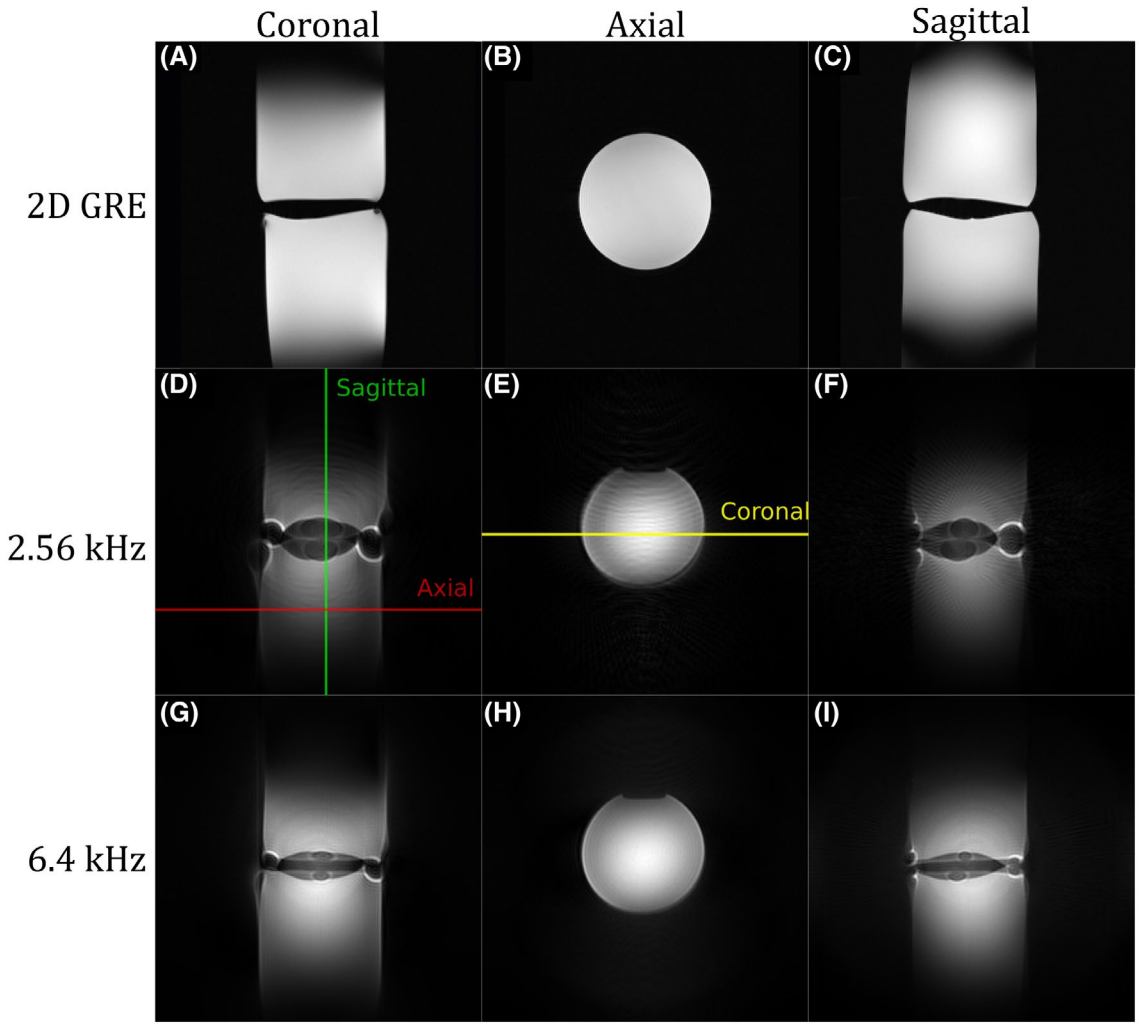

FIGURE 5 A-C, are reference 2D GRE images with FOV 250 × 250 mm, 256 × 230 matrix size, and 81.92 kHz bandwidth. cSWIFT images D-F, acquired with 2.56 kHz bandwidth and G-I, acquired with 6.4 kHz bandwidth

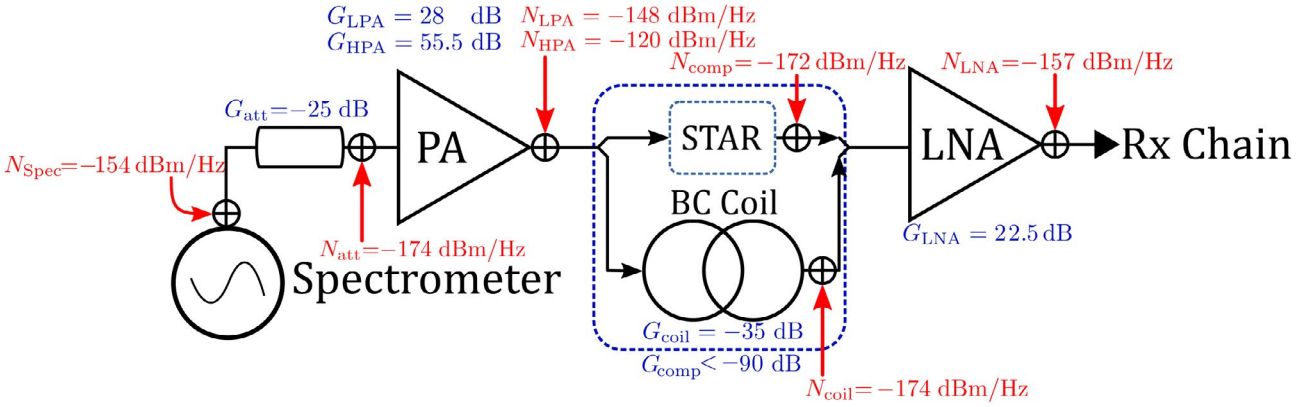

FIGURE 6 Gains and output referred noise powers are annotated on the system schematic. Gains and noise spectral density of LPA, HPA, and LNA, as well as gain of the coil and noise spectral density of the vector modulator is measured with a network analyzer and noise figure meter, and also verified with spectrum analyzer measurements

higher imaging bandwidth for both eliminating the transmit noise and minimizing the leak coupled to the received signal. This can be achieved by matching the frequency response of the vector modulator with the frequency response of the leak, or multiple vector modulators can be used to cancel at several frequencies to increase the apparent bandwidth. In the case

the bandwidth issue is solved, further improvement to the isolation amount can be done by increasing the number of bits in the attenuators.

From Equation (7), it can be seen that reducing amplifier noise output also reduces sufficient isolation. However, unless the noise output of the transmit amplifier is comparable to the spectrometer noise amplified by the transmit amplifier gain, it will not be the dominant factor determining the sufficient isolation. This conclusion implies that there is no need to invest in a low noise amplifier for the transmitter, whereas the amplifier's gain plays an important role.

TABLE 1 Noise spectral density close to the center frequency of 123.25 MHz for each experiment

	Experiment	Calculated (dBm/Hz)	Measured (dBm/Hz)
	1	−150.5	−150.3
	2	−132.3	−132
lLPA	3	−126.8	−126.5
	4	−149.3	−146.8
	5	−149.6	−148.6
lHPA	3	−115.7	−116.2
	4	−129.1	−129
	5	−149.6	−148.8

Note: Power spectral densities are calculated from the portions of power spectrum selected by hand.

Usage of an equal combiner at the receiver side incurs a 3 dB signal loss. In the future, this ratio should be selected so that less SNR impact is incurred on the signal. Since the vector modulator has an insertion loss of −18 dB and the passive isolation provides around 35 dB, a combiner ratio of 90% to 10% can be used, which should render SNR loss due to the combiner negligible, as discussed in Zhou et al.[26] Decreasing the contribution of the compensation path with this way also has the advantage that the noise of the vector modulator has a smaller contribution since it also gets attenuated by the combiner, which means less care is needed when designing the device. The vector modulator topology used in this work is digitally controlled, and its noise contribution decreases the SNR by an additional 1 dB.

The estimation error in the circuit output hinders the possibility of eliminating iterations. The current model, as explored in Appendix, disregards the reflections and nonlinearity occurring in the circuitry. For future work, it is possible to estimate the modeling error ($\epsilon(\boldsymbol{x})$) by using several measurements with arbitrary control input ($\boldsymbol{x}$) and fitting to the error between measurement and output estimation ($\hat{a}(\boldsymbol{x})$) or directly fitting a complex nonlinear function to the measurements ($m_i(x)$) itself. By eliminating iterations in this way, it will be possible to turn the cancellation process into real-time.

In the case of STAR imaging, noise is not the only factor that affects image quality. For example, vibrations arising from the

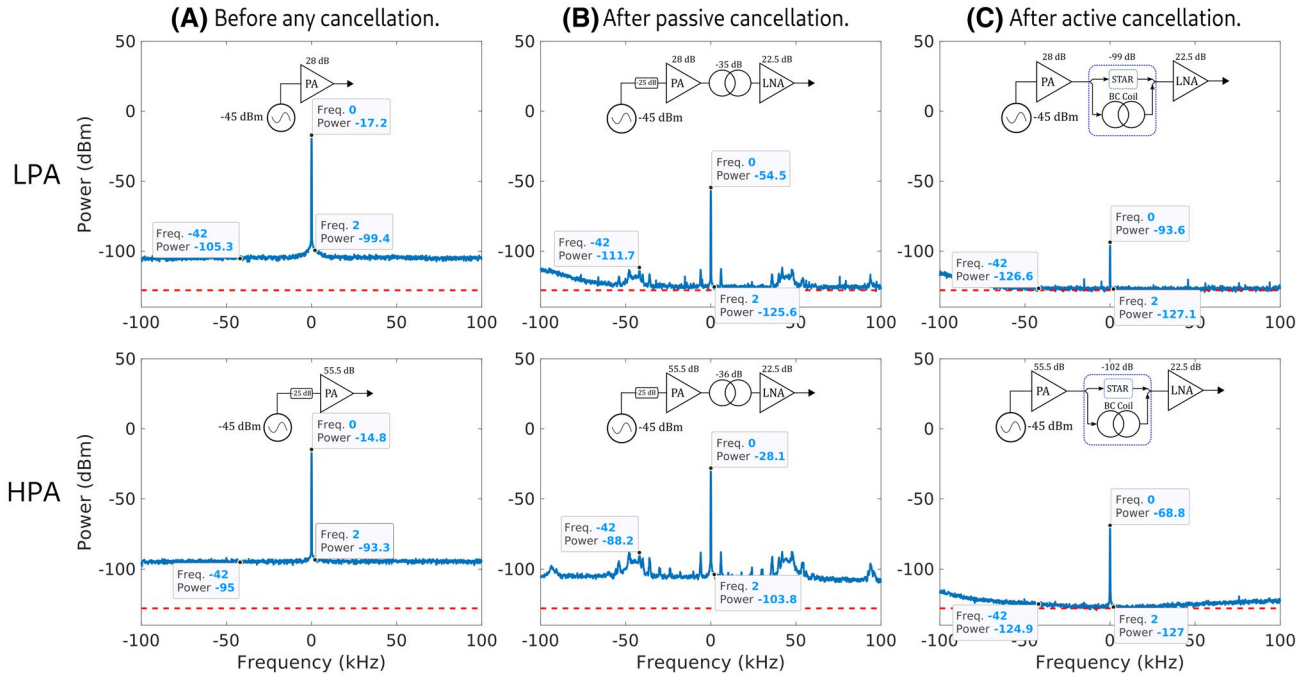

FIGURE 7 Noise PSD for the noise experiments (experiments 3, 4, and 5) and amplifiers LPA and HPA, acquired with a resolution bandwidth of 150 Hz at room temperature. Red dashed line marks the minimum achievable noise level. A, Low-frequency (~5.6 kHz) harmonics that can be seen in LPA and HPA are coupling from the power supply of custom amplifiers. Phase noise can also be observed as the spread around the center frequency. B, After passive isolation (~35 dB), it can be observed that both noise and spurs are reduced significantly. Since thermal noise is also reduced, some peaks that were not visible became visible. C, After active isolation with, most peaks are cleared out

gradient switching affect the performance of the cancellation by modulating the coupling between the transmit and receive coils, and they result in artifacts in the final image. Using a volume coil as opposed to small loop coils grants stability, yet vibrations are observed on the residual signal envelope. In this work, the problem was circumvented by switching the gradients on 5 ms before the acquisition. More elegant solutions can be incorporated in the future to solve these issues, such as real-time tracking and compensation of the leak signal even during the reception via an independent receive chain.

6 | CONCLUSION

In this work, noise in STAR imaging is analyzed, and the trade-offs between the parameters of the STAR system and the transmit chain are laid-out as a guideline for future applications of STAR in MRI. Furthermore, it is shown that the transmit noise can be reduced with cancellation in the analog domain. It should be possible to use the conventional transmit chains with high gain and high noise for STAR imaging by employing an active cancellation scheme with high enough isolation, if the cancellation system employed supports the power and linearity requirements. This can enable higher flip angles and alleviates the need for replacing the transmit amplifier. It is shown that there is sufficient isolation needed for achieving thermal noise at the receive side. After sufficient isolation is attained, removing the residual signal in post-processing does not impose SNR loss. Since the residual signal was not removed in the post-processing in this work, mild artifacts related to it can be seen in the images. With the possibility of using conventional amplifiers, STAR imaging can be possible with less scanner modification. The isolation threshold for the STAR system can be selected according to transmit system parameters and imaging bandwidth. In the future, for practical applicability, the low cancellation bandwidth problem needs to be solved either by matching the vector modulators frequency response to that of the leak signal or employing several vector modulators to isolate the leak at several frequencies. As the bandwidth increases, since the time available for excitation will decrease, a higher nutation frequency might be needed. We observed that gradient induced vibrations modulate the coupling coefficient. We solved this problem by introducing a gradient-dead time which increases the scanning time. By mechanically isolating the object, the gradient-dead-time and therefore the scanning time can be decreased.

This analysis is verified with a low-noise vector modulator structure in combination with the previously proposed algorithm. The algorithm is also described in detail and analyzed. It can be claimed that the algorithm can enable real-time cancellation of time-varying leak signals coming from the transmit chain. The algorithm offers the flexibility of further improvement, and it can be used for many different types of digitally controlled cancellation circuits. In the future, the proposed design can circumvent the issues causing the time-varying leak signal, such as load variation, temperature changes, etc., which will also allow STAR imaging of the moving tissues, such as chest and abdomen.

ORCID

Bilal Tasdelen http://orcid.org/0000-0001-6462-3651

REFERENCES

1. Bloch F, Hansen WW, Packard M. The nuclear induction experiment. *Phys Rev*. 1946;70:474-485.
2. Anderson WA. Applications of modulation techniques to high resolution nuclear magnetic resonance spectrometers. *Rev Sci Instrum*. 1962;33:1160-1166.
3. Robson MD, Gatehouse PD, Bydder M, Bydder GM. Magnetic resonance: an introduction to ultrashort TE (UTE) imaging. *J Comput Assist Tomogr*. 2003;27:825-846.
4. Bergin CJ, Pauly JM, Macovski A. Lung parenchyma: projection reconstruction MR imaging. *Radiology*. 1991.
5. Bergin CJ, Noll DC, Pauly JM, Glover GH, Macovski A. MR imaging of lung parenchyma: a solution to susceptibility. *Radiology*. 1992;183:673-676.
6. Hafner S. Fast imaging in liquids and solids with the Back-projection Low Angle ShoT (BLAST) technique. *Magn Reson Imaging*. 1994;12:1047-1051.
7. Wu Y, Ackerman JL, Chesler DA, Li J, Neer RM, Wang J, Glimcher MJ. Evaluation of bone mineral density using three-dimensional solid state phosphorus-31 NMR projection imaging. *Calcif Tissue Int*. 1998;62:512-518.
8. Madio DP, Lowe IJ. Ultra-fast imaging using low flip angles and fids. *Magn Reson Med*. 1995;34:525-529.
9. Kuethe DO, Caprihan A, Fukushima E, Waggoner RA. Imaging lungs using inert fluorinated gases. *Magn Reson Med*. 1998;39:85-88.
10. Weiger M, Pruessmann KP, Hennel F. MRI with zero echo time: hard versus sweep pulse excitation. *Magn Reson Med*. 2011;66:379-389.
11. Idiyatullin D, Corum C, Park JY, Garwood M. Fast and quiet MRI using a swept radiofrequency. *J Magn Reson*. 2006;181:342-349.
12. Idiyatullin D, Corum C, Moeller S, Garwood M. Gapped pulses for frequency-swept MRI. *J Magn Reson*. 2008;193:267-273.
13. Sohn SM, Vaughan JT, Lagore RL, Garwood M, Idiyatullin D. In vivo MR imaging with simultaneous RF transmission and reception. *Magn Reson Med*. 2016;76:1932-1938.
14. Özen AC, Bock M, Atalar E. Active decoupling of RF coils using a transmit array system. *Magn Reson Mater Phys Biol Med*. 2015;28:565-576.
15. Özen AC, Atalar E, Korvink JG, Bock M. In vivo MRI with concurrent excitation and acquisition using automated active analog cancellation. *Sci Rep*. 2018;8.
16. Salim M, Ozen AC, Bock M, Atalar E. Active decoupling of transmit and receive coils for full-duplex MRI. 2018. arXiv:1810.10973 [physics].
17. Idiyatullin D, Suddarth S, Corum CA, Adriany G, Garwood M. Continuous SWIFT. *J Magn Reson*. 2012;220:26-31.
18. Lee RF, Giaquinto RO, Hardy CJ. Coupling and decoupling theory and its application to the MRI phased array. *Magn Reson Med*. 2002;48:203-213.

19. Mahmood Z, Guérin B, Adalsteinsson E, Wald LL, Daniel L. An automated framework to decouple pTx arrays with many channels. Proceedings of the International Society for Magnetic Resonance in Medicine, Utah, USA, 21; 2013:1.
20. Mahmood Z, McDaniel P, Guérin B, Keil B, Vester M, Adalsteinsson E, Wald LL, Daniel L. General design approach and practical realization of decoupling matrices for parallel transmission coils. *Magn Reson Med*. 2016;76:329-339.
21. Bharadia D, McMilin E, Katti S. Full duplex radios. *ACM SIGCOMM Computer Communication Review, Hong Kong, China*. 2013:375-386.
22. Barneto CB, Riihonen T, Turunen M, Anttila L, Fleischer M, Stadius K, Ryynänen J, Valkama M. Full-duplex OFDM radar with LTE and 5G NR waveforms: challenges, solutions, and measurements. *IEEE Trans Microw Theory Tech*. 2019;1-13.
23. Salim M, Atalar E. *Full-duplex MRI for zero TE imaging*. The Department of Electrical and Electronic Engineering; 2016.
24. Tasdelen B, Sadeghi-Tarakameh A, Yilmaz U, Atalar E. Dynamic Decoupling for Simultaneous Transmission and Acquisition in MRI. Proceedings of the International Society for Magnetic Resonance in Medicine, 27, Montreal, May; 2019.
25. Montanari D, Castellano G, Kargaran E, Pini G, Tijani S, Caro DD, Strollo AGM, Manstretta D, Castello R. An FDD wireless diversity receiver with transmitter leakage cancellation in transmit and receive bands. *IEEE J Solid-State Circuits*. 2018;53:1945-1959.
26. Zhou J, Chakrabarti A, Kinget PR, Krishnaswamy H. Low-noise active cancellation of transmitter leakage and transmitter noise in broadband wireless receivers for FDD/co-existence. *IEEE J Solid-State Circuits*. 2014;49:3046-3062.
27. Emara M, Rosson P, Roth K, Dassonville D. A full duplex transceiver with reduced hardware complexity. *GLOBECOM 2017—2017 IEEE Global Communications Conference, Singapore*, December; 2017:1-6.
28. Tasdelen B, Sadeghi-Tarakameh A, Yilmaz U, Atalar E. Noise analysis for simultaneous transmission and reception enabled MRI scanner. In Proceedings of the ISMRM & SMRT Virtual Conference & Exhibition. 2020;28.
29. Garwood M, Idiyatullin D, Corum CA, et al. Capturing signals from fast-relaxing spins with frequency-swept MRI: SWIFT. *eMagRes*. American Cancer Society; 2012.
30. Motchenbacher CD, Connelly JA. *Low-noise electronic system design*. New York: Wiley; 1993.
31. Phillips J, Kundert K. Noise in mixers, oscillators, samplers, and logic an introduction to cyclostationary noise. Proceedings of the IEEE 2000 Custom Integrated Circuits Conference (Cat. No.00CH37044), Orlando, FL, USA; 2000:431-438.
32. Kouznetsov KA, Meyer RG. Phase noise in LC oscillators. *IEEE J Solid-State Circuits*. 2000;35:5.
33. Lee T, Hajimiri A. Oscillator phase noise: a tutorial. *IEEE J Solid-State Circuits*. 2000;35:326-336.Conference Name: IEEE Journal of Solid-State Circuits.
34. Flanagan M, Zimmerman G. Spur-reduced digital sinusoid synthesis. *IEEE Trans Commun*. 1995;43:2254-2262.
35. Kozlov M, Turner R. Fast MRI coil analysis based on 3-D electromagnetic and RF circuit co-simulation. *J Magn Reson*. 2009;200:147-152.
36. Sadeghi-Tarakameh A, Kazemivalipour E, Gundogdu U, Erdogan S, Atalar E. Accelerating the co-simulation method for the design of transmit array coils for MRI. *Magn Reson Mater Phys*. 2020.
37. Okada Y, Kawai T, Enokihara A. Design method of unequal Wilkinson power divider using LC-ladder circuits for multi-way power dividers. *2016 Asia-Pacific Microwave Conference (APMC), New Delhi, India*. 2016:1-4.
38. Okada Y, Kawai T, Enokihara A. Compact lumped-element 5-way wilkinson power divider with broadband operation. *2016 46th European Microwave Conference (EuMC), London, UK*. 2016:202-205.
39. Corum CA, Idiyatullin DS, Moeller S, Garwood MG. inventors. University of Minnesota, assignee. Multistep correction for angle consistent artifacts in radial sampled datasets. *US20130084023A1*. 2013.
40. Jackson J, Meyer C, Nishimura D, Macovski A. Selection of a convolution function for Fourier inversion using gridding (computerised tomography application). *IEEE Trans Med Imaging*. 1991;10:473-478.Conference name: IEEE transactions on medical imaging.
41. Electromagnetic compatibility and Radio spectrum Matters (ERM); Short Range Devices (SRD); Medical Body Area Network Systems (MBANSs) operating in the 2 483,5 MHz to 2 500 MHz range; Part 1: Technical characteristics and test methods. European Standard (ETSI); 2014.

APPENDIX A

DECOUPLING ALGORITHM

In this appendix, the details of the decoupling algorithm is given. The look-up table construction, which is referred to as constellation in this work, and cancellation steps can be found below. By understanding how the cancellation works and examining the noise sources, isolation performance can be increased via tweaking the algorithm or modeling the circuit better, which in turn may improve the noise performance.

Constellation construction

Following steps can be carried to construct constellation:

1. Each branch's input is swept from state 1 to N while the other lines kept at state 1 and S_{21} of the output is recorded. In this case the measurements can be formulated as:

$$m_i(x) = \sum_{k \neq i, k=1}^{M} a_k(N) + a_i(x) + l_{\text{cal}} \tag{A1}$$

Here, $m_i(x)$ is the measurement of the circuit output for branch i at state x, $a_k(x)$ is the complex coefficient of branch k and l_{cal} is the coupled signal coming from the coil connected to the circuit during calibration, if any. Note that for this work, there are 128^4 set of states in total, since there are 128 states ($N = 128$) and 4 branches ($M = 4$). However, due to time constraints, we are only measuring $128 \cdot 4$ different

set of states, just enough to solve the model. How the left-out measurements are estimated is explained in the step 2.

2. Complex coefficients that are not measured in step 1 to reduce the data collection time are estimated from the measured set as linear combinations of each branch. Complex coefficients in the constellation ($\hat{a}(\boldsymbol{x})$) are calculated for a circuit with M delay line and N states, and for state vectors $\boldsymbol{x} = \{x_i \,|\, x_i \in 1, \cdots, N, i \in 1, \cdots, M\}$ as given in Equation (A2):

$$\hat{a}(\boldsymbol{x}) = \sum_{k=1}^{M} m_k(x_k) \tag{A2}$$

3. The constellation is sorted by the phase and it is categorized into sections where in each section phases of the coefficients are in some interval with the length of $\Delta\phi$. In this way, the initial index of these sections that contain the coefficients with the phases in $[k \cdot \Delta\phi, (k+1) \cdot \Delta\phi)$ are stored, for any k that satisfies $\frac{-\pi}{\Delta\phi} \leq k < \frac{\pi}{\Delta\phi}, k \in Z$.

4. The coefficients in each of these sections are sorted by their amplitudes separately. Similar to the previous step, they are categorized by their magnitude this time into subsections. The indices that point to the boundaries of these subsections are stored in another LUT. It will be used to jump directly to the vicinity of the estimations that have the phase and the amplitude values close to the desired signal.

In this work, the LUT was referred to as constellation, since it represents the normalized output values that can be achieved by the circuit. Once the constellation is known, the cancellation loop can be carried out, as in Figure A1.

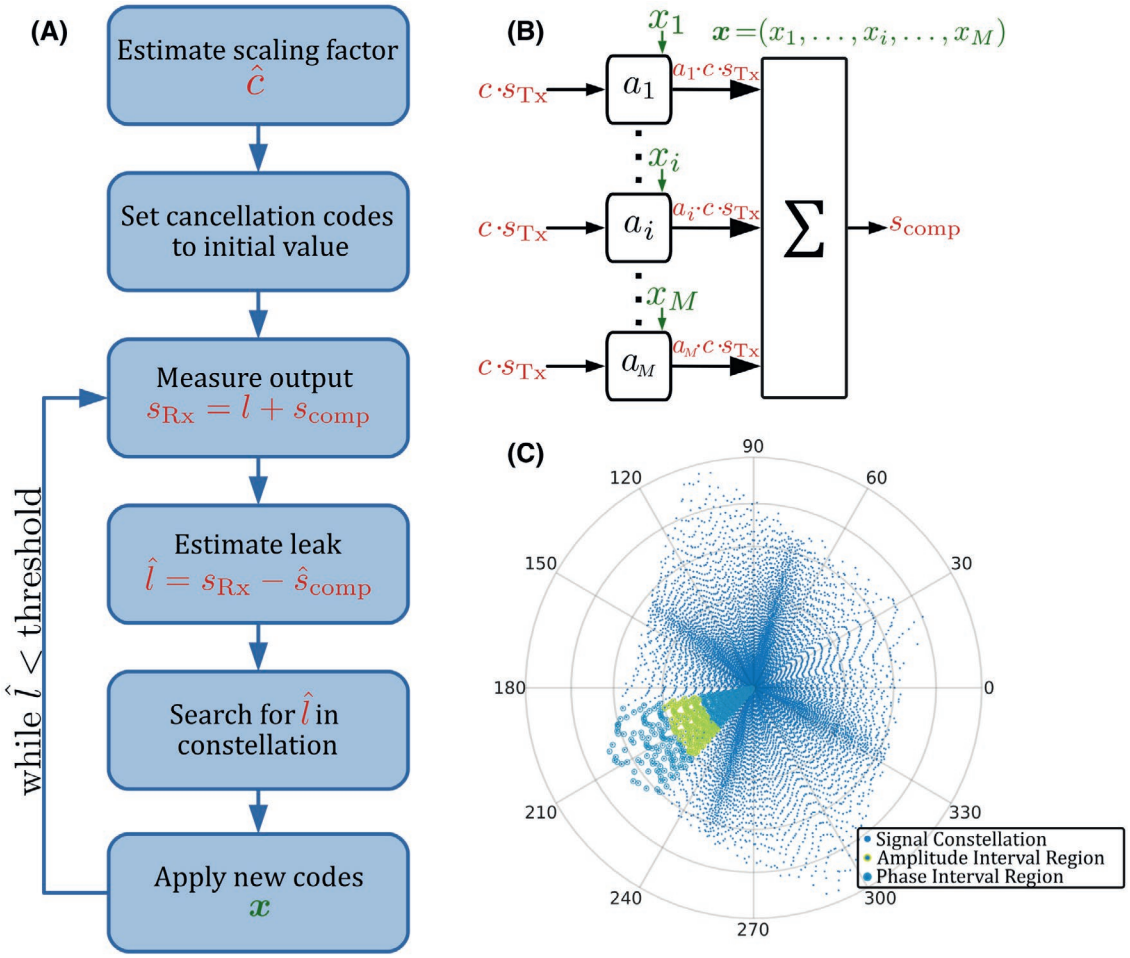

FIGURE A1 The decoupling algorithm. A, Flowchart of the compensation loop. $\hat{c}$, $\hat{l}$ and $\hat{s}_{\mathrm{comp}}$ can be considered as estimated $X(f)$, $L(f)$, and $Y(f, \boldsymbol{x})$ at the center frequency, respectively. B, Model assumed on the vector modulator. In other terms, the output s_{comp} is the weighted combination of the input $c \cdot s_{Tx}$ by the complex weight a_i of each line. C, A representative visualization of the constellation. Each point represents the value of the transfer function at the center frequency for a given $\boldsymbol{x}$ vector. A subsection divided according to the phase and the amplitude can be seen as the yellow part

We analyze the error sources of $\hat{a}(\boldsymbol{x})$ in the estimation by inserting Equation (A1) into Equation (A2):

$$\hat{a}(\boldsymbol{x}) = \sum_{k=1}^{M} a_k(x_k) + K \tag{A3}$$

$$K = (M-1) \cdot \sum_{k=1}^{M} a_k(N) + M \cdot l_{\text{cal}} \tag{A4}$$

Following these equations, estimated coefficients can be written in terms of actual coefficients as follows:

$$\hat{a}(\boldsymbol{x}) = a(\boldsymbol{x}) + \epsilon(\boldsymbol{x}) + K + n_i \tag{A5}$$

Note that K is a constant that adds bias to all estimated superposed signals in the constellation. $\epsilon(\boldsymbol{x})$ can be considered a distortion of the estimate or modeling error depending on the input vector $\boldsymbol{x}$, and n_i is the measurement noise coming from $m_i(x)$.

Cancellation loop

Let the output measurement of the system at iteration k be $\overline{m}_k(\boldsymbol{x}_k)$, where $\boldsymbol{x}_k$ is the input vector to the STAR circuit at the iteration k. If we omit the complex scaling factor due to the gain and phase addition of the overall system, $\overline{m}_k(\boldsymbol{x}_k)$ can be written as:

$$\overline{m}_k(\boldsymbol{x}_k) = l_k + a(\boldsymbol{x}_k) \tag{A6}$$

where l_k is the leak signal, and $a_k(\boldsymbol{x}_k)$ is the output of the STAR circuit at iteration k.

From the constellation, an estimate of $a(\boldsymbol{x}_k)$, $\hat{a}(\boldsymbol{x}_k)$ is known. Hence, the leak signal at iteration k can be estimated using:

$$\hat{l}_k = \overline{m}_k(\boldsymbol{x}_k) - \hat{a}(\boldsymbol{x}_k) \tag{A7}$$

For iteration $k+1$, we choose the input vector $\boldsymbol{x}_{k+1}$ so that:

$$\hat{a}(\boldsymbol{x}_{k+1}) + q_{k+1} = -\hat{l}_k \tag{A8}$$

where q_{k+1} is the error coming from the discrete nature of constellation and $\hat{a}(\boldsymbol{x}_{k+1})$ is selected as close as possible to $\hat{l}_k$ to cancel out the leak signal.

If we insert Equation (A6) and (A7) into Equation (A8), we get:

$$\hat{a}(\boldsymbol{x}_{k+1}) = -l_k - a(\boldsymbol{x}_k) + \hat{a}(\boldsymbol{x}_k) - q_{k+1} \tag{A9}$$

From Equation (A5), we can further expand the equation by replacing $\hat{a}(\boldsymbol{x}_k)$ as:

$$\hat{a}(\boldsymbol{x}_{k+1}) = -l_k + \epsilon(\boldsymbol{x}_k) + K - q_{k+1} \tag{A10}$$

By also replacing $\hat{a}(\boldsymbol{x}_{k+1})$ and reorganizing the equation, we get:

$$a(\boldsymbol{x}_{k+1}) + l_k = \epsilon(\boldsymbol{x}_k) - \epsilon(\boldsymbol{x}_{k+1}) - q_{k+1} \tag{A11}$$

There are 2 critical remarks in Equation (A11). The first one is the constant error in the model coming from K cancels out during the feedback loop and does not affect the performance. The second is the residual leak, which is determined by quantization error q and difference in the modeling error $\epsilon(\boldsymbol{x})$ in iteration k and $k-1$. In the case that this difference is zero, the algorithm needs only 2 iterations to converge. In the realistic case that the difference is non-zero, the algorithm iterates until this difference is smaller than the threshold. This observation suggests that a model with a smaller $\epsilon(\boldsymbol{x})$ is required to increase the convergence rate. However, although the output model used in the algorithm is not perfect, it is possible to achieve more than 80 dB isolation in this way, as can be seen in Figure 4.